Measurement of the $^{19}F(p,\gamma)^{20}Ne$ reaction and interference terms from $E_{c.m.} = 200$–760 keV

A. Couture,* M. Beard, M. Couder, J. Görres, L. Lamm, P. J. LeBlanc, H. Y. Lee,† S. O'Brien, A. Palumbo, E. Stech, E. Strandberg, W. Tan, E. Uberseder, C. Ugalde,‡ and M. Wiescher
Nuclear Science Laboratory, University of Notre Dame, Notre Dame, Indiana 46556, USA

R. Azuma§
Department of Physics, University of Toronto, Toronto, Ontario, Canada M55 1A7
(Received 6 September 2007; published 10 January 2008)

The $^{19}F(p,\gamma)^{20}Ne$ reaction represents the only breakout path for the carbon-nitrogen-oxygen cycle operating at temperatures below $T = 0.1$ GK, an energy regime important for main-sequence hydrogen burning as well as hydrogen burning in asymptotic giant branch stars. Large experimental uncertainties exist due to unknown low energy direct and resonant reaction contributions that have been difficult to study because of the high γ-ray background from the $^{19}F(p,\alpha_2\gamma)$ reaction. A new detection technique has been developed at the University of Notre Dame to measure the $^{19}F(p,\gamma)$ and $^{19}F(p,\alpha_i\gamma)$ reactions over an energy range of $E_{c.m.} = 200$–760 keV. The analysis was carried out in a Breit-Wigner framework. This allowed a new determination of the resonance parameters as well as a first measurement of the signs of the interference terms. Partial widths and resonance strengths are reported for the resonances in this region.

DOI: 10.1103/PhysRevC.77.015802 PACS number(s): 25.40.Lw, 25.40.Ny, 26.20.−f, 27.30.+t

I. INTRODUCTION

The cold carbon-nitrogen-oxygen (CNO) cycle is a catalytic hydrogen-burning sequence on carbon, nitrogen, and oxygen seed material converting the existing hydrogen fuel to helium. The CNO cycle is illustrated in Fig. 1. For the CNO cycle to compete with the primary p-p chain reactions, the temperatures must exceed 20 MK, corresponding to stars of 1.5 $M_\odot$ or greater mass [1]. In addition to the catalytic fusion of four hydrogen nuclei to form helium, the abundance of the catalyst isotopes are changed depending on the associated CNO reaction rates. The net CNO mass fraction, however, remains constant unless a breakout reaction sequence causes a leak toward the Ne-Na mass region. The only reaction that can potentially remove the catalytic material from the cycle at lower temperatures is $^{19}F(p,\gamma)^{20}Ne$ [2]. This reaction is expected to be rather weak compared to the the $^{19}F(p,\alpha)^{16}O$ reaction, so most of the ^{19}F produced by the CNO cycle will be recycled back to ^{16}O, with no material breaking out to ^{20}Ne [3].

Very limited measurements have been performed in the past because the 6.125-MeV γ-ray background from the $^{19}F(p,\alpha\gamma)$ reaction is quite large, making measurements of the weak $^{19}F(p,\gamma)$ cross section extremely difficult. Previous measurements relied on detecting the >11 MeV primary transition to the first excited state of ^{20}Ne [4–9]. Most of these prior measurements relied on low resolution and relatively small-volume NaI(Tl) detectors. All of the measurements were susceptible to pileup from the 6.125-MeV γ rays from the competing $(p,\alpha_i\gamma)$ reactions as the energy resolution was insufficient to separate the two components. Subotić [9] and Clifford [8] made the only measurements that employed a high-resolution Ge(Li) detector. Due to the low detection efficiency for the high-energy γ rays from $^{19}F(p,\gamma)$, the Subotić measurement was limited to observing on-resonance components [9]. Significant discrepancy was observed between the published results of the different measurements, particularly of the strength of a broad resonance. One measurement observed an anomalously high partial width for the broad resonance at $E_{c.m.} = 564$ keV [7]. The measurement by Clifford [8] was restricted to the energy range from $E_{c.m.} = 470$ keV to $E_{c.m.} = 670$ keV and saw no evidence of the resonance reported at $E_{c.m.} = 564$ keV. None of the measurements were sufficiently sensitive to determine the signs of the interference components that were expected to contribute almost 50% to the reaction rate at stellar temperatures [10,11]. Based on the presently available data the branching ratio between the $^{19}F(p,\alpha)^{16}O$ and the $^{19}F(p,\gamma)^{20}Ne$ channel is quite uncertain. The possible loss of CNO material ranges between 0.01 and 1.0% of the produced ^{19}F [2]; this difference is not negligible because over extended periods of hydrogen burning substantial amounts of ^{20}Ne and other isotopes in the NeNa cycles may accumulate due to the cyclic nature of the process [2]. It therefore is important to remove the present uncertainties by a measurement of the low energy $^{19}F(p,\gamma)^{20}Ne$ cross section.

II. EXPERIMENTAL PROCEDURE

A. Beam and target production

The measurements were made at the University of Notre Dame Nuclear Science Laboratory. The JN model Van de Graaff accelerator was used to produce proton beams of energies from 200 to 700 keV, corresponding to $E_{c.m.} =$

*acouture@lanl.gov; Presently at Los Alamos Neutron Science Center, Los Alamos National Laboratory, Los Alamos, New Mexico 87545.
†Presently at Argonne National Laboratory, Argonne, Illinois 60439.
‡Presently at The Department of Physics and Astronomy, University of North Carolina, Chapel Hill, North Carolina, 27599, USA.
§Also at The Department of Physics, The University of Notre Dame, Notre Dame, Indiana, 46556, USA.

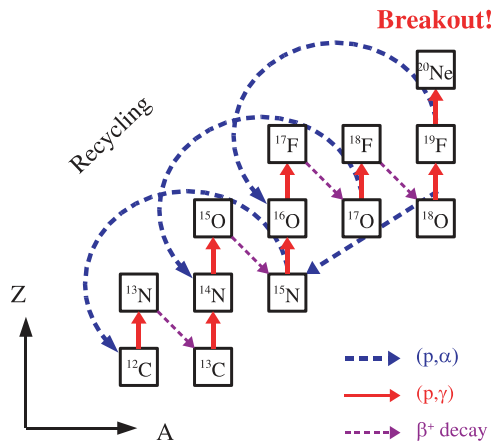

FIG. 1. (Color online) The CNO cycle operating at temperatures below 0.1 GK.

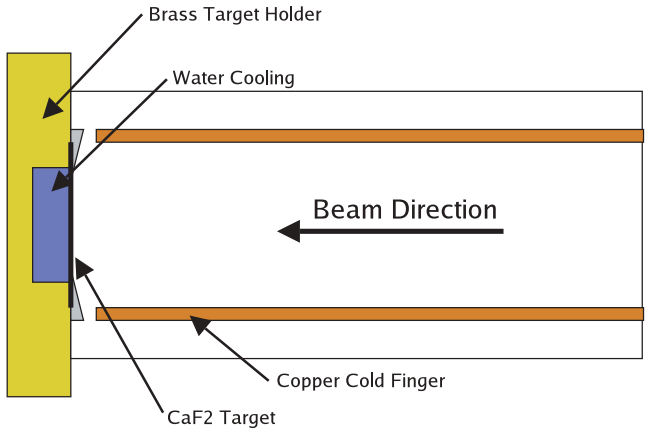

FIG. 2. (Color online) The target holder is shown above. The beam impinges from the right. The copper cold finger was biased to −300 V and cooled with liquid nitrogen. This froze out any carbon in the beam as well as ensured accurate charge collection. The CaF_2 target was on a metal backing that was water cooled. The water flow lines are not indicated.

190–665 keV. The KN accelerator was used to produce protons from 600 to 800 keV ($E_{\text{c.m.}} = 570$–760 keV), ensuring a broad overlap region, including the strong resonance at $E_{\text{c.m.}} = 634$ keV. All of the experiments were carried out on the same beamline, with only the accelerator providing beam to the target changing. The beam was wobbled over a 0.8×0.8 cm area.

The targets were prepared by evaporation of CaF_2 powder onto 0.25-mm-thick tantalum or nickel backings. There was a separation of 11 cm between the evaporation boat and the target backing to ensure target homogeneity. Target thicknesses for a majority of the targets used in the experiment were $\approx 25\ \mu g/cm^2$. This corresponds to a target thickness of ≈8 keV for 480-keV protons. This generally gave reasonable count rates and still allowed a clear separation of the resonances. Significantly thicker targets ($\approx 80\ \mu g/cm^2$ corresponding to ≈24 keV for 480-keV protons) were used to verify the results observed in the inter-resonance region from 320 to 460 keV. The target thickness was measured using the narrow $E_{\text{c.m.}} = 460$ keV resonance. A full discussion of the target preparation an properties can be found in Ref. [12].

Because beam-stop targets were used, the charge was collected on target and used to determine the total number of protons. A cold finger biased to −300 V was used to prevent carbon buildup and ensure reliable charge collection (see Fig. 2). Degradation of the fluorine was observed in the target and corrections were made for this effect. The degradation was monitored throughout the experiment by monitoring the $(p, \alpha_2\gamma)$ yield of the 460-keV resonance. The degradation consisted of both a loss in total number of fluorine atoms, which appeared to behave linearly with accumulated charge, and a sputtering of CaF_2 from the surface of the target, all of which occurred in the first few μC of beam on target. Although the total number of fluorine atoms decrease linearly with accumulated charge, the calcium content seemed to be constant after the first few μC. There was no evidence of an energy dependence of the degradation. The target degradation was parametrized as a function of accumulated charge and initial target conditions. Further details of the corrections for target degradation are given in Ref. [12]. The target parametrization is shown in Figs. 3 and 4.

B. Detection array

Significant advances have been made in detector technologies since the previous measurements had been made, making available large volume, segmented HPGe detectors. To take full advantage of this, a hybrid detection system was designed that could exploit the high efficiency of large-volume NaI(Tl) detectors with the high resolution offered by HPGe detectors. Four 8-inch-diameter and 6-inch-tall cylindrical NaI(Tl) detectors were used together with a HPGe clover detector. Each of the four crystals in the clover had a relative efficiency of approximately 22%. The detectors were arranged as is shown in Fig. 5. The HPGe detector was positioned directly in front of the target holder, mounted at 0° to cover the largest possible

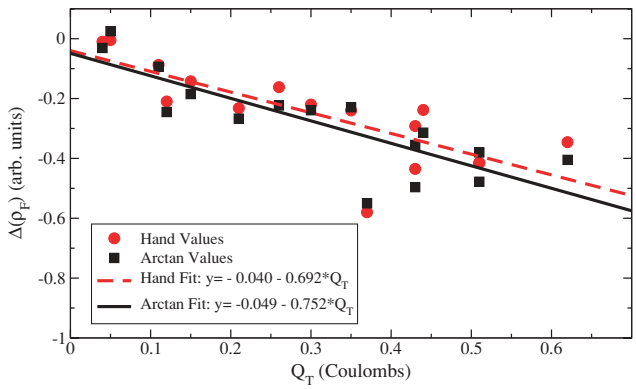

FIG. 3. (Color online) The parametrization of the fluorine density is shown above. The vertical axis is the change in fluorine density measured from the yield of the (p, α_2) reaction over the 460-keV resonance. The horizontal axis is the total accumulated charge. The two different data sets are from different methods of determining the height but are generally in good agreement. Although the trend is well reproduced, there is still significant scatter in the data, which is why a large uncertainty was assigned to the correction. Both fits are least-squares fits.

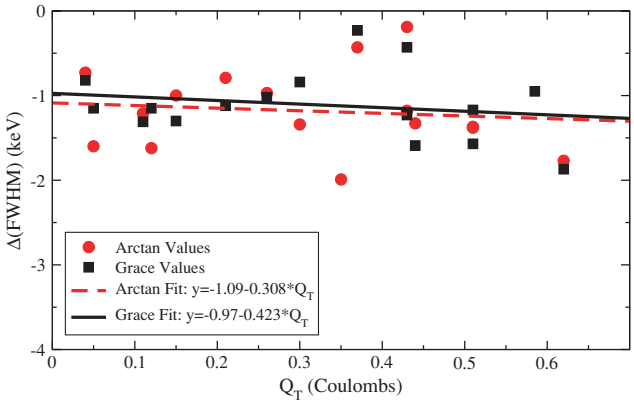

FIG. 4. (Color online) The parametrization of the target thickness, or FWHM, is shown above. The vertical axis shows the change in the FWHM measured over the 460-keV resonance, whereas the horizontal axis shows total accumulated charge. Note that in contrast to the fluorine density, the target thickness shows relatively little dependence on accumulated charge after the first burst. Once again, the two data sets correspond to different methods of determining the width of the excitation function. The fits are least-squares fits.

solid angle. The segmentation of the HPGe clover allowed an instantaneous count rate in each crystal of as much as 15 kHz. The four NaI(Tl) detectors were mounted at backward angles and rotated 45° in ϕ and θ to offer an improved solid angle coverage and to maximize detection efficiency.

A Q-value gating technique was developed to optimize the detection of the ^{19}F(p, γ) reaction. The decay scheme of ^{20}Ne is shown in Fig. 6. The array was optimized to observe the 1.63 MeV transition from the first excited state to the ground state in the HPGe detector while observing the high-energy primary transition in the NaI(Tl) detectors. A coincidence

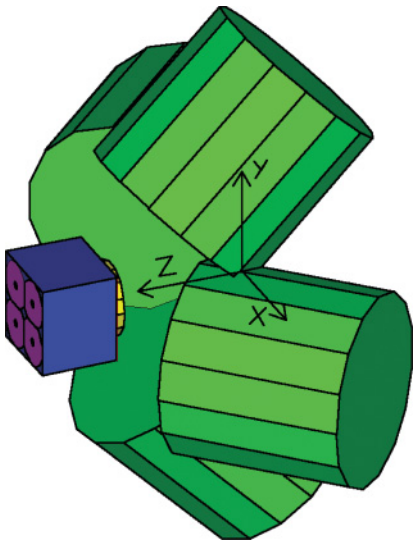

FIG. 5. (Color online) A schematic of the detector array used is shown above. The HPGe detector is on left, centered and mounted at 0° with respect to the beam. The NaI(Tl) detectors are primarily at backward angles, rotated to provide maximum solid angle coverage. The beam path was collinear with the positive z axis.

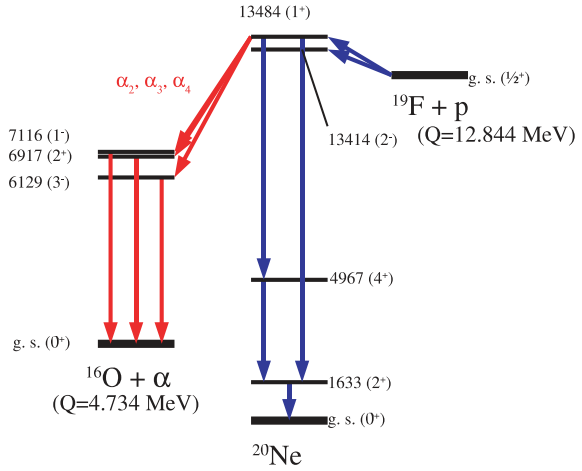

FIG. 6. (Color online) The decay scheme for ^{20}Ne states populated by proton capture is shown above. The γ decays proceed dominantly to the first excited state. α emission to the ground state of ^{16}O are inhibited by angular-momentum conservation.

requirement was placed between the NaI(Tl) detectors and the HPGe crystals, and a sum energy $\geqslant$10 MeV was required for valid events. Because the Q value is 12.484 MeV, this energy condition was high enough to filter out most of the 6- to 7-MeV γ-ray lines from the concurrent $(p, \alpha_i\gamma)$ reactions. Small corrections to the efficiency were made for the slight beam energy dependence introduced by the fixed threshold. Further details can be found in Ref. [12]. If both conditions were met, then the 1.63-MeV γ-ray yield was measured in the HPGe clover. By requiring the coincidence in hardware, it was possible to run at rates of 10–12 kHz in the individual HPGe detectors while still only requiring acquisition at a rate of 4 kHz, keeping the live time well above 80%. The effectiveness

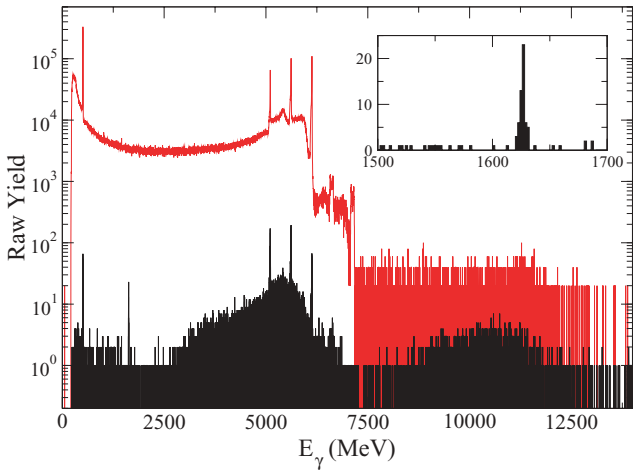

FIG. 7. (Color online) The suppression of the $(p, \alpha\gamma)$ components by the array is shown above. In red (light) is shown the yield seen by the HPGe clover with no cuts or conditions. In black (dark) is the yield after the multiplicity and Q-value cuts. The inset shows the region surrounding the 1.63 MeV first-excited state decay of ^{20}Ne in greater detail. The vertical scale in the large picture is logarithmic, whereas the inset shows only the suppressed data on a linear scale. A suppression of close to 10^4 was achieved.

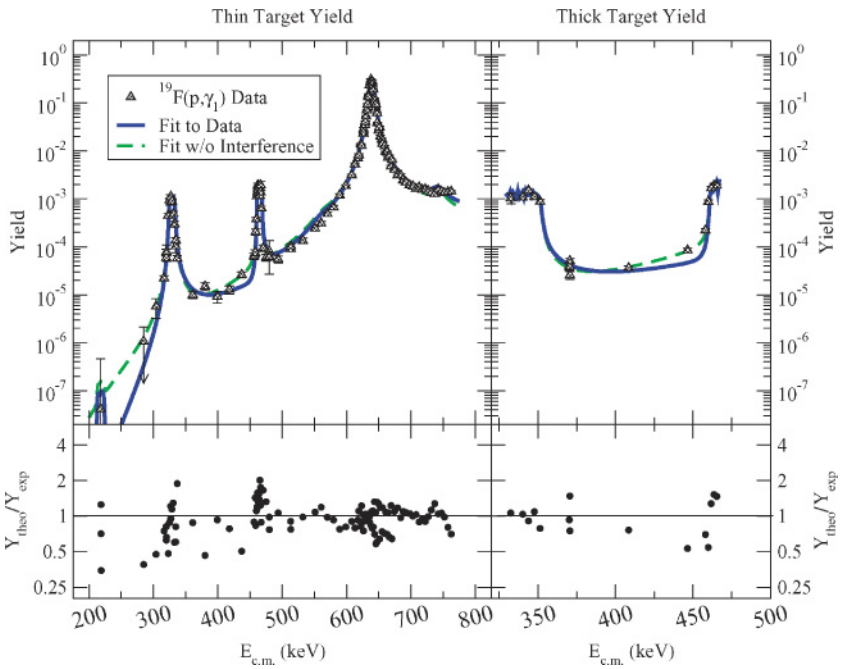

FIG. 8. (Color online) The (p, γ_1) yield data are shown above. Also shown is a predicted yield for an ideal target, 8 keV thick for the plot on the left and 24 keV for the plot on the right. The deviations between the fit and the experimental data shown below the plot include target degradation effects. The agreement between the data and the fit is quite good. On the panel on the right is shown the fit to the thick target data. The ratio of the calculated yield to the observed yield is shown at the bottom. The data points near 220 keV are all upper limits.

of these gating conditions is shown in Fig. 7. At the same time, 1 of every 20 events in the germanium detector was passed through to the acquisition regardless of coincidence so the $(p, \alpha\gamma)$ yield could be monitored simultaneously with the (p, γ). These two features proved to be essential as they provided rapid feedback on the energy and resonance structure as well as allowed running at high beam currents to see the (p, γ) reaction channel.

III. ANALYSIS

Experimental yield curves were measured for the (p, γ_1), $(p, \alpha_2\gamma)$, $(p, \alpha_3\gamma)$, and $(p, \alpha_4\gamma)$ channels. The (p, γ_2) reaction was also monitored, but no significant yield was observed outside of the $E_{\text{c.m.}} = 634$ keV resonance. The resonance energies, spins, and parities are well known [13], so no effort was made to determine them. The yield curves were fit with a set of Breit-Wigner resonance shapes. Interference terms were calculated for the resonances. Following Refs. [14,15] the angle-independent total yield was calculated with

$$Y = \sum_i \left[\int_{E-\chi}^{E} \frac{\sigma_i(E)}{\varepsilon(E)} \mathrm{d}E \right] + \sum_{i<j} \left[\delta_{J_i^\pi}^{J_j^\pi} \int_{E-\chi}^{E} \frac{2\kappa_{i,j}\sqrt{(\sigma_i \sigma_j)}}{\varepsilon(E)} \cos\left(\varphi_{R_i} - \varphi_{R_j}\right) \mathrm{d}E \right], \tag{1}$$

where the sum is over resonances i, the cross sections were Breit-Wigner cross sections [16], χ is the target thickness in terms of energy, $\varepsilon(E)$ is the energy loss of the beam, l is the channel angular momentum, φ_R is the resonance phase shift, and $\delta_{J_i^\pi}^{J_j^\pi}$ is the Kronecker δ function, restricting the interference to terms with the same J^π. The term $\kappa_{i,j}$ can take values of $+1$ and -1 and determines whether the interference is constructive or destructive. Cases for which $\kappa_{i,j} = +1$ are constructive at zero energy. The energy loss $\varepsilon(E)$ was calculated from the stopping powers determined by Ziegler and Biersack [17]. For energies far from the resonance energy, the energy dependence of the partial widths becomes an important effect and is given by

$$\Gamma(E) = \Gamma_R \frac{P_l(E)}{P_l(E_R)}, \tag{2}$$

where $P_l(E)$ is the penetrability for energy E with angular momentum l calculated for a radius of $1.4A^{\frac{1}{3}}$ fm. The penetrabilities for both the ingoing and outgoing particles were calculated and their effect on the yield was included. As was mentioned in Sec. II A, the target profile was parametrized so the target thickness integration reflected the target thickness and fluorine density as each data point was being taken. Equation (1) is the integration of the cross section given by

$$\sigma_T(E) = \sum_i \sigma_i(E) + \sum_{i<j} \delta_{J_i^\pi}^{J_j^\pi} 2\kappa_{i,j}\sqrt{\sigma_i \sigma_j} \cos\left(\varphi_{R_i} - \varphi_{R_j}\right). \tag{3}$$

Because of the geometry, the observed yield is a total yield, not an angular-dependent yield. Thus the cross section contains only interference terms from resonances with the same J^π. The total phase shift is determined by the resonant phase shift, the Coulomb phase shift, and the hard sphere shift, but the Coulomb phase shift and hard sphere phase shift are independent of resonance energy, depending only on l and E [18]. The only phase-shift term that remains is the resonant phase shift, given by Eq. [18] as

$$2\tan\varphi_R = \frac{\Gamma}{E_R - E}. \tag{4}$$

Because the phase shift is defined as the argument of the tangent function, care must be taken in choosing the appropriate range $(0 < \varphi_R < \pi)$ so the function behaves properly.

The numerical integration was completed using numerical techniques from the *cernlib* package [19]. The partial widths were allowed to vary freely and minimized with the *Minuit* minimization package [20]. The sign of the interference term, which has to be determined experimentally, was changed manually to find the optimal fit. All four reaction channels were fit simultaneously.

The total width was calculated from the partial widths and thus varied through the partial widths. A background state was included to simulate the contributions of all higher-lying resonances though it contributed significantly only in the (p,γ) yield. Fits to two of the yield curves can be seen in Figs. 8 and 9. As can be seen, the yield is well reproduced. By requiring a simultaneous fit of the thick and thin target data as well as a fit over all of the data sets, it was possible to obtain self-consistent resonance parameters. The uncertainty in the data is solely from the statistical uncertainty in the yield at each point. By fitting the entire excitation function, the minimization gains the benefit of the full function shape. The resonance parameters are given in Table I. The measured signs of the interference terms are given in Table II.

Although previous measurements were generally normalized to the strength of 634 keV resonance, in this measurement the absolute efficiency of the HPGe clover was determined both by use of a ^{60}Co source as well as by looking at decays from the $E_x = 12.239$ MeV state of ^{28}Si populated via the ^{27}Al(p,γ) reaction. The resonance strength was taken from Lyons [21], whereas the branching ratios were taken from Meyers [22]. Previous measurements of the resonance parameters for ^{19}F(p,γ) have relied on either a published measurement of the cross sections ([5–7,9]) of resonances in ^{19}F(p,γ) or the yield relative to the ^{19}F(p,α) reaction ([4]). Even more problematic, uncertainties are not reported by previous authors for the these resonance parameters. Because neither previous measurements of this reaction nor the references that were used for calibration [23–25] provide uncertainties, it is not possible to determine the systematic uncertainty of these measurements. Although careful measurements have been made of several of the resonances [26–28], including some that were designed to place certain resonances on a sufficiently firm footing to use them as standards [29], no recent simultaneous measurements of multiple reaction channels have been made. As a result, a perusal of the the typical compilations reveals that there are significant discrepancies in the total and partial widths of the states [13,30]. Because all of the reaction channels that contributed significantly to the total width were measured simultaneously, the decision was made to make an independent absolute detection efficiency determination and then allow all of the resonance parameters to vary freely to best fit the data. The $E_x = 12.239$ MeV state in ^{28}Si was chosen because the energies of the γ decays were similar to the γ-ray energies from the decay of the states in ^{20}Ne* and ^{16}O*. Summing corrections were accounted for in the determination of the absolute efficiency. The methodology is described in Ref. [31] while the details are given in Ref. [12]. The determination of the coincidence efficiency was made by comparing the singles yield to the coincidence yield for the 634-keV resonance in ^{19}F(p,γ). GEANT [32] simulations were made to determine the change in coincidence efficiency

TABLE I. Measured resonance parameters.

Γ_p (eV)	Γ_{γ_1} (eV)	Γ_{α_2} (eV)		Γ (keV)
	$E_{R,\mathrm{c.m.}} = 213$ keV $J^\pi = 2^-$			
Present	$\mathbf{0.890^{1346}_{-265}}$ [a]	$\mathbf{0.011^{+0.003}_{-0.002}}$	**<0.06**	$\mathbf{882^{+1346}_{-265}}$
$(p,\alpha_{2,3,4})$ [b]	0.94±0.02	–	–	1000
	$E_{R,\mathrm{c.m.}} = 323$ keV $J^\pi = 1^+$			
	Γ (keV)	Γ_p (eV)	Γ_{γ_1} (eV)	Γ_{α_2} (eV)
Present	**2.08±0.34**	$\mathbf{35.8^{+5.6}_{-5.4}}$	$\mathbf{0.107^{+0.024}_{-0.019}}$	$\mathbf{1971^{+369}_{-294}}$
(p,p_0) [c]	2.8	45	–	–
(p,p') [d]	2.8	–	–	–
(p,γ_1) [e]	–	–	0.28±0.06	–
$(p,\alpha_{2,3,4})$	2.22±0.04	–	–	2800
	$E_{R,\mathrm{c.m.}} = 460$ keV $J^\pi = 1^+$			
Present	**1.050±0.225**	$\mathbf{12.1^{+1.7}_{-1.7}}$	$\mathbf{0.276^{+0.053}_{-0.041}}$	$\mathbf{743^{+185}_{-169}}$
(p,p')	2.1	–	–	–
(p,γ_1)	–	–	0.42	–
$(p,\alpha_{2,3,4})$	0.86±0.03	–	–	700
	$E_{R,\mathrm{c.m.}} = 564$ keV $J^\pi = 2^-$			
Present	**37.4±7.0**	$\mathbf{45.9^{+7.1}_{-7.3}}$	**<2**	$\mathbf{37100^{+7670}_{-6060}}$
(p,p_0)	35	42	–	–
(p,p')	35	–	–	–
(p,γ_1)	29±3	–	12	–
$(p,\alpha_{2,3,4})$	24±3	–	–	–
	$E_{R,\mathrm{c.m.}} = 634$ keV $J^\pi = 1^+$			
Present	**6.67±1.15**	$\mathbf{6530^{+1320}_{-1040}}$	$\mathbf{1.27^{+0.27}_{-0.25}}$	$\mathbf{70.7^{+14.1}_{-13.8}}$
(p,p_0)	7.1	7000	–	–
(p,p')	7.1	–	–	–
(p,γ_1)	5.7±0.7	–	2.2	–
$(p,\alpha_{2,3,4})$	6.4±0.3	–	–	–

[a] Due to the large asymmetry in the uncertainties for Γ_{α_2}, which dominates the total width, the covariance matrix method will not properly represent the uncertainties, so the asymmetric uncertainty in the dominant partial width has been used.
[b] [30]Table 20.29.
[c] [30]Table 20.25.
[d] [30]Table 20.26.
[e] [30]Table 20.24.

TABLE II. Measured interference signs $\kappa_{i,j}$.

^{19}F(p,γ_1) $(J^\pi = 1^+)$				
$\kappa_{i,j}$	$j = 323$	$j = 460$	$j = 634$	$j \approx 3$ MeV
$i = 323$		−1	−1	+1
$i = 460$			−1	+1
$i = 634$				−1
^{19}F(p,α_2) $(J^\pi = 1^+)$				
$\kappa_{i,j}$	$j = 323$		$j = 460$	$j = 634$
$i = 323$			+1	−1
$i = 460$				−1
^{19}F(p,α_2) $(J^\pi = 2^-)$				
$\kappa_{i,j}$	$j = 213$		$j = 564$	$j = 741$
$i = 213$			+1	+1
$i = 564$				−1

as a function of the γ-ray energy. It is worth noting that a previous measurement had been done to place the ^{19}F$(p,\alpha_2\gamma)$ reaction at $E_{\text{c.m.}} = 323$ keV on sufficiently firm status as to make it a reference strength [29]. The value determined in this measurement of $\omega\gamma = 25.5 \pm 5.5_{\text{fit}} \pm 4.1_{\text{syst}}$ eV is in good agreement with the value of $\omega\gamma = 22.3 \pm 0.8$ eV determined by Becker *et al.* [29] using a ^{19}F beam and a hydrogen gas target. The value determined in this measurement of $\Gamma_{\gamma_1} = 1.27^{+0.27}_{-0.25\,\text{fit}} \pm 0.20_{\text{syst}}$ eV is significantly different from the value of 2.2 eV determined by Ref. [4] and commonly used as a reference for the ^{19}F(p,γ) reaction.

IV. UNCERTAINTY ATTRIBUTION

There were several factors that contributed to the final uncertainty in the deduced resonance parameters. For the discussion, these will be separated into fitting uncertainties, which will generally affect the shape of the excitation function, and systematic uncertainties, which generally affect the overall normalization of the the parameters.

A significant advantage of the *Minuit* minimization package is that the uncertainty of minimized parameters can be obtained directly from *Minuit*. The statistical uncertainty of the measured value on a point-by-point basis is included in this uncertainty. Because what is being fit is a global shape, including multiple reaction channels, it is possible, and even likely, that the final uncertainty in the fit will be less than the average uncertainty of an individual point, a compelling factor in the decision to try to obtain full excitation functions. Furthermore, because multiple reaction channels were measured simultaneously, it is to be expected that some of the uncertainties are correlated. *Minuit* calculates a full covariance matrix, allowing the uncertainty in derived quantities such as the resonance strength and total width to be properly determined (see Ref. [33] or a similar text on the treatment of correlated variables). Finally, *Minuit* also offers the possibility to calculate asymmetric uncertainties using the *minos* routine. The statistical error for a given data point was calculated by assuming that it and the background followed a Poisson distribution and adding the individual errors in quadrature. Normalization errors due to the charge collection were neglected as these corrections would have typically been less than 1%.

The sources of the systematic errors in the measurement were more varied and provided the largest uncertainty in the measurement. The two largest uncertainties came from the correction for the target profile and degradation and the uncertainty in the resonance strength of the ^{27}Al(p,γ) resonance used to determine the absolute efficiency of the detector array. Additional sources of uncertainty came from the determination of the coincidence efficiency and the calculation of summing corrections.

The reported resonance strength $\omega\gamma$ for the $E_{\text{c.m.}} = 655$ keV resonance in ^{27}Al(p,γ) was 0.65 ± 0.08 eV [21]. Gamma-rays of 1776, 2838, 4827, 7424, 7632, and 10447 keV were used from the decay of the the $E_x = 12.239$ MeV state of ^{28}Si as well as the 1332.5- and 1173.2-keV γ rays from a ^{60}Co source were used to determine the photopeak efficiencies for the four γ rays of interest from the decay of ^{20}Ne (1663, 6129, 6917, and 7116 keV). The single and double escape peak efficiency was determined for γ rays with $E_\gamma > 3$ MeV. This was important because the yield in the $(p,\alpha_{2,3,4})$ channels was partly determined from the escape γ rays. The uncertainty in the resonance strength results in a 12% uncertainty in the absolute efficiency for the γ rays of interest.

TABLE III. Budget of errors for systematic uncertainties.

Source	Uncertainty (%)
Target parameterization	10
Efficiency determination	12
Coincidence efficiency	3
Summing corrections	2
Total systematic	16

The second major source of systematic uncertainty came from the characterization of the target. As was mentioned in Sec. II A, the fluorine content deteriorated over the course of the measurements. This deterioration was measured at discrete intervals and then parametrized as a function of accumulated charge. The parametrization of the fluorine density, or plateau height, is shown in Fig. 3, whereas the parametrization of the target thickness, or full-width half-maximum (FWHM), is shown in Fig. 4. Although the uncertainty in the linear fit to the data was less than 2%, it is reasonable to expect some deviations from a linear behavior in a given target due to slight physical differences in the targets and limits in the reproducibility of the target profile. For this reason, an uncertainty of 10% was assigned to the fluorine content and profile.

Other uncertainties included the correction for the coincidence efficiency (3%) as well as uncertainty in the summing corrections that were made to calculate the efficiency of the HPGe detector (2%). Table III summarizes the systematic uncertainties.

V. RESULTS AND IMPLICATIONS

The selectivity of the measurement for the different signs of the interference terms is illustrated in Fig. 10. This shows only the (p,γ_1) channel and changes in sign for the $J^\pi = 1^-$ states. Because the statistics were significantly better for the $(p,\alpha_2\gamma)$ channel, even better discrimination was observed. A full fit optimization was completed for each of the sign combinations. The χ^2 values are listed in Table IV. It is worth noting that due

TABLE IV. χ^2/N versus interference signs $\kappa_{i,j}$.

$\kappa_{323,460}$	$\kappa_{323,634}$	$\kappa_{460,634}$	χ^2/N
+1	+1	+1	21.12
+1	+1	−1	22.11
+1	−1	+1	20.93
+1	−1	−1	21.10
−1	+1	+1	21.18
−1	+1	−1	21.14
−1	−1	+1	21.26
−1	−1	−1	20.77

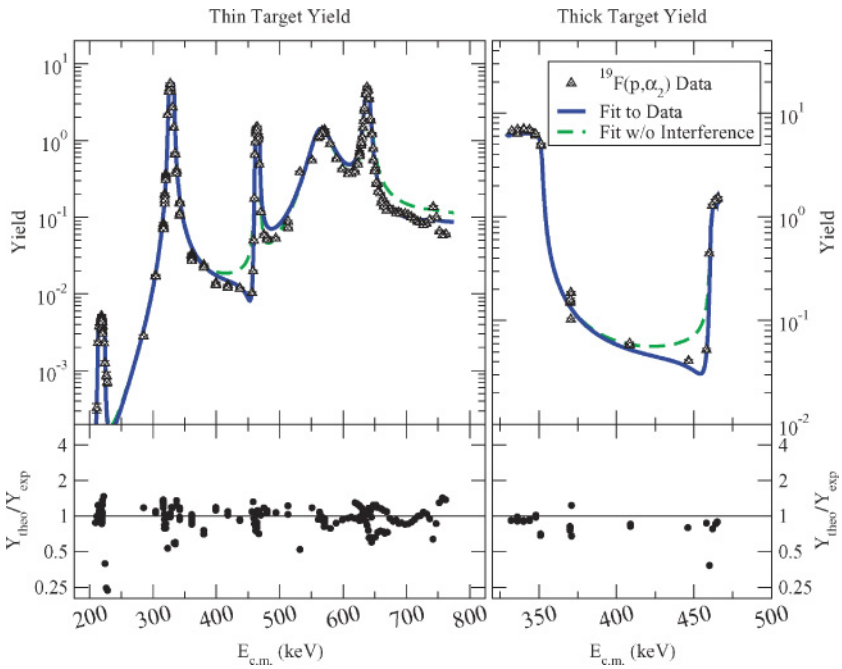

FIG. 9. (Color online) The $(p,\alpha_2\gamma)$ yield data are shown above. Again, the predicted yield illustrated is based on an ideal target, whereas the fit and deviations include target degradation effects. The acquisition method allowed the α-particle channel data to be taken simultaneously with the γ-ray channel data, which was of significant advantage in the fitting of the data and improved systematics. The thick target yield and fit are shown in the panel on the right.

to the higher uncertainties in the (p,γ_1) channel, it contributed only approximately 10% of the final χ^2, so the few percentages variation in χ^2 is actually quite significant.

To properly fit the high-energy side of the 634-keV resonance, it was necessary to include a broad, high-energy 1^+ state to account for the contribution of all higher-lying resonances. The properties of this background state were not well constrained by the present data, and although these uncertainties had little effect on the resonance properties in the region studied, they are sufficient to cause large uncertainties on the S factor at astrophysically interesting regions (30–120 keV). To try to determine the sensitivity of the data to the position and width of the broad background state, the minimization was completed with the energy and width of the state fixed at several values around the optimal value. Shown in Fig. 11 is a contour plot of χ^2 for those values. As can be seen, the minimum is extremely shallow, indicating that the state is not at all constrained by the present data. At 50 keV, the corresponding S factor ranges from just over 100 to over 500 keV-b for these different scenarios. Clearly, there is a very strong dependence on the background term, indicating that further measurements at higher energies are necessary, particularly of the possible $T = 1$ resonance at $E_{c.m.} = 1.35$ MeV [13], to constrain this background term.

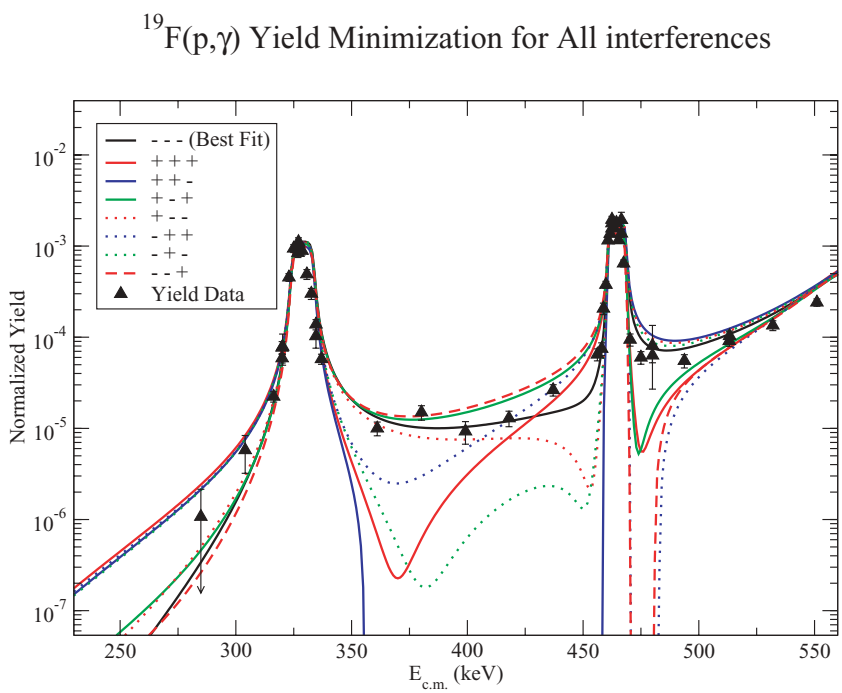

FIG. 10. (Color online) Shown are the different predicted yield curves produced after a complete minimization was done with indicated set of interference signs. A target thickness of 8 keV for 480-keV protons was assumed for the calculations. The interferences varied were $\kappa_{323,460}$, $\kappa_{323,634}$, and $\kappa_{460,634}$, respectively. The best fit is shown in black. Because the interference has very little effect near the resonance energy, the energy region highlighted is between the 323- and 460-keV resonances. The yield predictions for different interferences are indistinguishable at higher energies as the yield is dominated by the direct contribution of the 634-keV state. Note how critical quality data in this region off resonance is for selecting between different interference sign combinations.

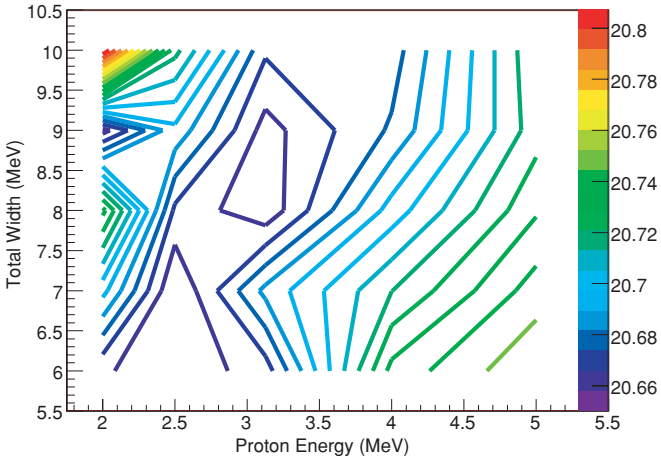

FIG. 11. (Color online) Shown is a contour of the χ^2 space around the minimum for several fixed energies and total widths for the broad background state. Note that although there is a minimum, the variation in χ^2 per degree of freedom is less than 1% over the whole range of state parameters.

An additional measurement that would further constrain the data would be a measurement of the elastic scattering at these low energies. The lack of a proton-scattering data set to fit simultaneously with the other sets allowed more variation and, as a result, larger fitting uncertainties than would be desired. The dominant Coulomb scattering at these proton energies makes an elastic-scattering measurement challenging.

All of these effects suggest that the reaction rate will be lower than previously predicted, particularly the destructive interference observed below 300 keV. Angulo *et al.* [11] adopt a 50% uncertainty to their evaluated rate due to the lack of data on the presence and signs interference terms. This work recommends that the rate should be adjusted downward, consistent with the destructive interference observed, effectively closing the cold CNO cycle. A final determination of the stellar reaction rate and S factor will require further measurements at higher energies to constrain the role of the background state needed to properly fit the data. Plans for higher-energy measurements as well as a global analysis that would include reaction channels not studied in this work are underway. An analysis that includes the high-energy portion of the reactions studied here as well as data for $^{19}\mathrm{F}(p,\alpha_0)$ and $^{19}\mathrm{F}(p,\alpha_\pi)$ will conclusively determine the (p,α):(p,γ) branching at the end of the CNO cycle.

VI. SUMMARY

The new detection system has been a very effective tool to observe the $^{19}\mathrm{F}(p,\gamma)$ reaction. It is sufficiently sensitive to determine interference terms, even in regions of resonances in the competing channels, allowing the first clean measurement of a full excitation function, even in the inter-resonance regions. There was no observed strength for the lowest-lying resonance at $E_{\mathrm{c.m.}} = 213$ keV and an upper limit of $\Gamma_\gamma = 60$ meV was established. The broad resonance reported by [7] at $E_{\mathrm{c.m.}} = 564$ keV was not observed and an upper limit of $\Gamma_\gamma = 2$ eV was be established. For this reason, it does not contribute in any significant way to the astrophysical reaction rate. The resonance strengths for the other resonances were generally smaller than that previously reported, and the net interference effect at low energies was seen to be destructive in the $^{19}\mathrm{F}(p,\gamma)$ channel.

ACKNOWLEDGMENTS

The authors thank Mr. Bradley Mulder, Mr. James Kaiser, and Mr. Jerry Lingle for their technical assistance with the maintenance and operation of the accelerators at the Nuclear Science Laboratory at the University of Notre Dame. This work was supported by the National Science Foundation under grant no. PHY01-40324, the Joint Institute for Nuclear Astrophysics, NSF-PFC, under grant no. PHY02-16783, and the U.S. Department of Energy under the auspices of Los Alamos National Security, LLC, Department of Energy contract number DE-AC52-06NA25396.

[1] C. Rolfs and W. Rodney, *Cauldrons in the Cosmos* (University of Chicago Press, Chicago, 1988).
[2] M. Wiescher, J. Görres, and H. Schatz, J. Phys. G: Nucl. Part. Phys. **25**, R133 (1999).
[3] M. Arnould, N. Mowlavi, and A. E. Champagne, in *Stellar Evolution: What Should Be Done?*, edited by A. Noels, D. Fraipon-Caro, M. Gabriel, N. Grevasse, and P. Demarque (Université de Liège, 1995), 32nd Liège Inter. Astro. Coll., p. 17.
[4] R. M. Sinclair, Phys. Rev. **93**, 1082 (1954).
[5] G. K. Farney, H. H. Given, B. D. Kern, and H. T. M., Phys. Rev. **97**, 720 (1955).
[6] L. Keszthelyi, I. Berkes, I. Demeter, and I. Fodor, Nucl. Phys. **29**, 241 (1962).
[7] I. Berkes, I. Dézsi, I. Fodor, and L. Keszthelyi, Nucl. Phys. **43**, 103 (1963).
[8] E. T. Clifford, master's thesis, University of Toronto (1974).
[9] K. M. Subotić, R. Ostojić, and B. Z. Stepančić, Nucl. Phys. **A331**, 491 (1979).
[10] G. R. Caughlan and W. A. Fowler, At. Data Nucl. Data Tables **40**, 283 (1988).
[11] C. Angulo, M. Arnould, M. Rayet, P. Descouvemont, C. Leclercq-Willain, A. Coc, S. Barhoumi, P. Aguer, C. Rolfs, R. Kunz *et al.*, Nucl. Phys. **A656**, 3 (1999).
[12] A. Couture, Ph.D. thesis, University of Notre Dame (2005).
[13] F. Ajzenberg-Selove, Nucl. Phys. **A475**, 1 (1987).
[14] C. Rolfs and R. E. Azuma, Nucl. Phys. **A227**, 291 (1974).
[15] M. Wiescher, R. N. Boyd, S. L. Blatt, L. J. Rybarcyk, J. A. Spizuoco, R. E. Azuma, E. T. H. Clifford, J. D. King, J. Görres, C. Rolfs *et al.*, Phys. Rev. C **28**, 1431 (1983).
[16] H. E. Gove, in *Nuclear Reactions*, edited by P. M. Endt and M. Demeur (Interscience, New York, 1959), vol. 1, pp. 259–317.
[17] J. F. Ziegler and J. P. Biersack, SRIM-2003.26 (2003).
[18] A. J. Ferguson, *Angular Correlation Methods in Gamma-Ray Spectroscopy* (North-Holland, Amsterdam, 1965).

[19] CERN Development Team (2003).
[20] Application Software Group, *MINUIT-Function Minimization and Error Analysis*, CERN, Geneva, Switzerland (1998), CERN Program Library Long Writeup D506.
[21] P. B. Lyons, J. W. Toevs, and D. G. Sargood, Nucl. Phys. **A130**, 1 (1969).
[22] M. A. Meyer, I. Venter, and D. Reitmanm, Nucl. Phys. **A250**, 235 (1975).
[23] T. W. Bonner and J. E. Evans, Phys. Rev. **73**, 666 (1948).
[24] F. Ajzenberg-Selove and T. Lauritsen, Nucl. Phys. **11**, 1 (1959).
[25] F. Azjenberg-Selove, Nucl. Phys. **A190**, 1 (1972).
[26] J. F. Streib, W. A. Fowler, and C. C. Lauritsen, Phys. Rev. **59**, 253 (1941).
[27] W. A. Fowler and C. C. Lauritsen, Phys. Rev. **76**, 314 (1949).
[28] S. E. Hunt and W. M. Jones, Phys. Rev. **89**, 1283 (1953).
[29] H. W. Becker, W. E. Kieser, C. Rolfs, H. P. Trautvetter, and M. Wiescher, Z. Phys. A **305**, 319 (1982).
[30] D. R. Tilley, C. M. Cheves, J. H. Kelley, S. Raman, and H. R. Weller, Nucl. Phys. **A636**, 249 (1998).
[31] K. Debertin and R. G. Helmer, *Gamma- and X-ray Spectroscopy with Semiconductor Detectors* (North-Holland, Amsterdam, 1988).
[32] Application Software Group, *GEANT-Detector Description and Simulation Tool*, CERN, Geneva, Switzerland (1993), CERN Program Library Long Writeup W5013.
[33] P. R. Bevington and D. K. Robinson, *Data Reduction and Error Analysis for the Physical Sciences* (McGraw-Hill, New York, 1992), 2nd ed.